

# Ultrafast Lateral Photo-Dember Effect in Graphene Induced by Nonequilibrium Hot Carrier Dynamics

*Chang-Hua Liu,<sup>†</sup> You-Chia Chang,<sup>‡§</sup> Seunghyun Lee,<sup>†</sup> Yaozhong Zhang,<sup>⊥</sup> Yafei Zhang,<sup>⊥</sup>  
Theodore B. Norris,<sup>\*†,‡</sup> and Zhaohui Zhong<sup>\*†,‡</sup>*

<sup>†</sup> Department of Electrical Engineering and Computer Science, University of Michigan, Ann Arbor, Michigan 48109, USA

<sup>‡</sup> Center for Photonics and Multiscale Nanomaterials, University of Michigan, Ann Arbor, Michigan 48109, USA

<sup>§</sup> Department of Physics, University of Michigan, Ann Arbor, Michigan 48109, USA

<sup>⊥</sup> Key Laboratory for Thin Film and Microfabrication of the Ministry of Education, Research Institute of Micro/Nano Science and Technology, Shanghai Jiao Tong University, 800 Dongchuan Road, Shanghai 200240, China

## **Supplementary Section 1.**

### **Device structure and scanning photocurrent spectroscopy**

To fabricate graphene devices, graphene films were synthesised by chemical vapor deposition (CVD) method on copper foil and then transferred to the device substrate with pre-patterned local bottom back gate electrode (covered by 50 nm  $\text{Al}_2\text{O}_3$  as gate dielectric by atomic layer deposition). The source and drain contact electrodes for the graphene channel are separated by 5  $\mu\text{m}$ , and the contact metal is either palladium (60 nm) or titanium/gold (5/50 nm) deposited

by electron-beam evaporation. On top of the graphene channel, another 50 nm  $\text{Al}_2\text{O}_3$  film was deposited by atomic layer deposition. This top dielectric film also serves as a passivation layer.

The photoresponses of fabricated graphene devices are characterized using the scanning photocurrent spectroscopy<sup>1-3</sup> as schematically shown in Fig. S1. In this setup, a focused laser spot is raster scanned at the surface of a planar graphene transistor, and simultaneously, short circuit photocurrent generated from the transistor is detected by the lock-in amplifier. To monitor the spatial position of laser spot, a photodetector is incorporated into this setup to detect the intensity of reflection light from graphene device. Therefore, the mapping of photocurrent image with reflection image provides the spatial information of photoresponse from the graphene transistor.

When spatially probing the gate dependence of photoresponse, the focused laser spot is kept to scan along the certain cross section between source and drain contact under different gate voltages. The collected data is then demonstrated in our gate-dependent photocurrent maps (Fig. 2b-d) for comparison.

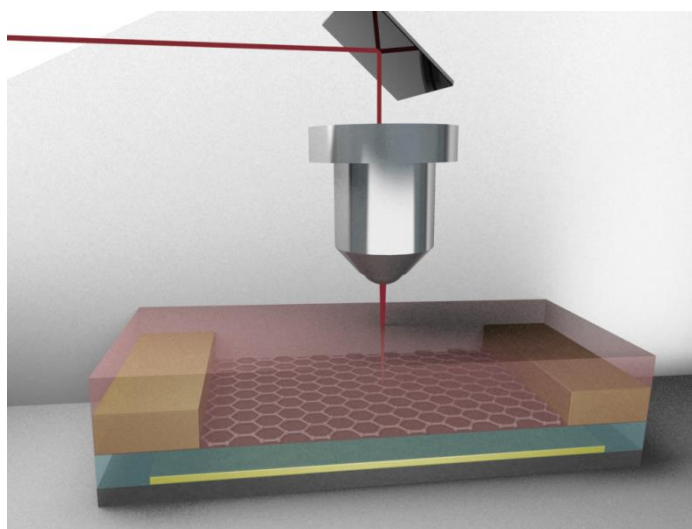


**Figure S1 Scanning photocurrent spectroscopy.** This figure schematically shows the setup of scanning photocurrent measurement.

## Supplementary Section 2.

### Gate-dependent photoresponse under low excitation pulse energy

The photoresponse induced by the photo-Dember field is the result of nonequilibrium hot carrier dynamics. Therefore, by reducing the pulse excitation power, photo-Dember field might not be the dominated mechanism for photocurrent generation due to the lower photocarrier temperature and photocarrier density. Here, we examine the photoresponse from the device A, device B and device C respectively with lower excitation pulse energy. As demonstrated in Fig. S2 a-c, the measured gate-dependent photocurrent from the metal/graphene interface displays polarity reversal. This feature suggests the photoresponse is not simply dominated by the photo-Dember field. Instead, the conventional mechanisms, including photovoltaic<sup>1-2</sup> and photo-thermoelectric effect<sup>4</sup>, could also play the crucial roles.

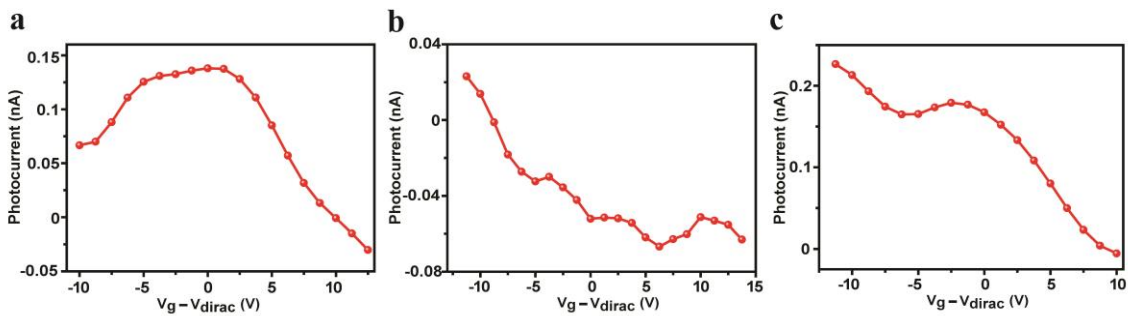


**Figure S2 Gate-dependent photocurrent under low excitation pulse energy.** The measured gate-dependent photocurrent generation from the metal/graphene interface from (a) Device A with the pulse energy at 2.63 pJ, (b) Device B with the pulse energy at 2.2 pJ and (c) Device C with the pulse energy at 0.66 pJ, respectively.

### Supplementary Section 3.

#### Simulation of Drift-Diffusion equations and modelling of hot carrier temperature

To simulate the dynamical distribution of hot carriers and the photo-Dember field, we solve the continuity equation and Poisson equation:

$$\frac{\partial n_i}{\partial t} = G \pm \mu_i \frac{\partial(n_i E)}{\partial x} + D_i \frac{\partial^2 n_i}{\partial x^2} - \frac{n_i}{\tau} \quad (1)$$

$$\frac{\partial E}{\partial x} = \frac{q(n_h - n_e)}{\epsilon_0 \epsilon_r} \quad (2)$$

where  $G$  represents photocarrier generation created by a femtosecond pulse,  $n$  is the density of photocarrier ( $i = e, h$  represent electrons and holes respectively),  $\mu$  is the photocarrier mobility,  $D$  is the photocarrier diffusion coefficient,  $\tau$  is the photocarrier lifetime,  $q$  is electron charge,  $\epsilon_0$  is vacuum permittivity and  $E$  is the photo-Dember electric field induced by the asymmetric distribution of excited electrons and holes. We assume the relative permittivity ( $\epsilon_r$ ) of graphene is 3 [5]. In addition,  $D$  is related to  $\mu$  via the Einstein relation<sup>6</sup>:

$$D = \frac{\mu k_B T}{2q} \quad (3)$$

where  $k_B$  is the Boltzmann constant and  $T$  is the temperature of photocarrier. To numerically solve the above equations, it is necessary to know the time evolution of photocarrier temperature. In this regard, we further solve the photocarrier-phonon coupled rate equations<sup>7</sup>. The simulated time evolution of photocarrier temperature after a pulse excitation is shown in Fig. S3, and with this result, we could model the dynamics of hot electrons, holes as well as the photo-Dember electric field for the given electron mobility ( $\mu_e$ ), hole mobility ( $\mu_h$ ) and excitation pulse energy.

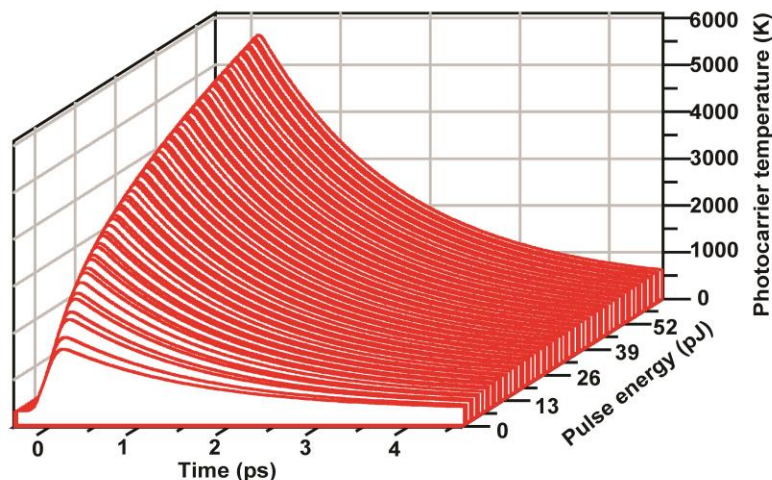


**Figure S3 Time evolution of photocarrier temperature.** The simulated time evolution of photocarrier temperature after a pulse excitation.

#### **Supplementary Section 4.**

##### **Power dependence of photocurrent generation under CW and pulse laser excitation**

Fig. S4a shows the power dependence of photocurrent generation from the metal/graphene interface under CW laser excitation. The result exhibits that the magnitude of photocurrent increases linearly with the excitation power. Notably, this observation is different from the result under pulse laser excitation (Fig. 3d, main text), suggesting the mechanism of photoresponse induced by CW excitation is different from pulse excitation.

Additionally, we performed photocurrent measurements under different excitation pulse fluences. The measured two devices here are different from the device shown in Fig. 3d of the main text. Both devices again show that photocurrent increases super-linearly with the excitation fluence, indicating photo-Dember effect is the dominant mechanism for photocurrent generation (Fig. S4b&c).

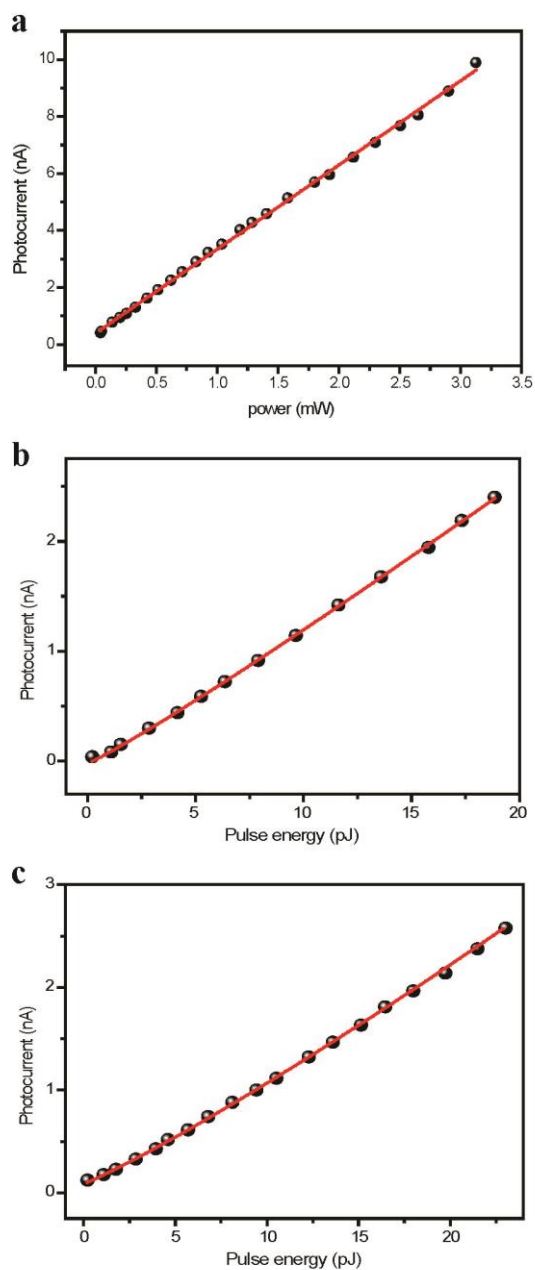


**Figure S4 Power dependence of photocurrent generation.** (a) The power-dependent photocurrents were detected by focusing the CW laser beam at the metal/graphene interface. The black round symbols are experimental results and the red line is a linear fit to the data. (b-c) Power-dependent photocurrents under pulse laser excitation. The black round symbols are

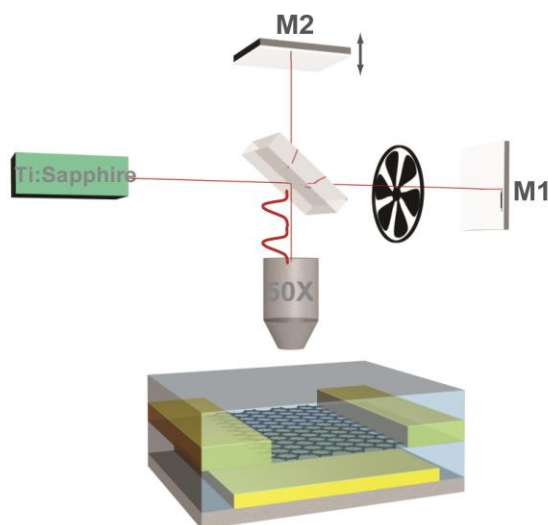
experimental results and the red lines represent power-law fit with (b)  $I_{pc} \propto P^{1.08}$  and (c)  $I_{pc} \propto P^{1.15}$  respectively.

## Supplementary Section 5.

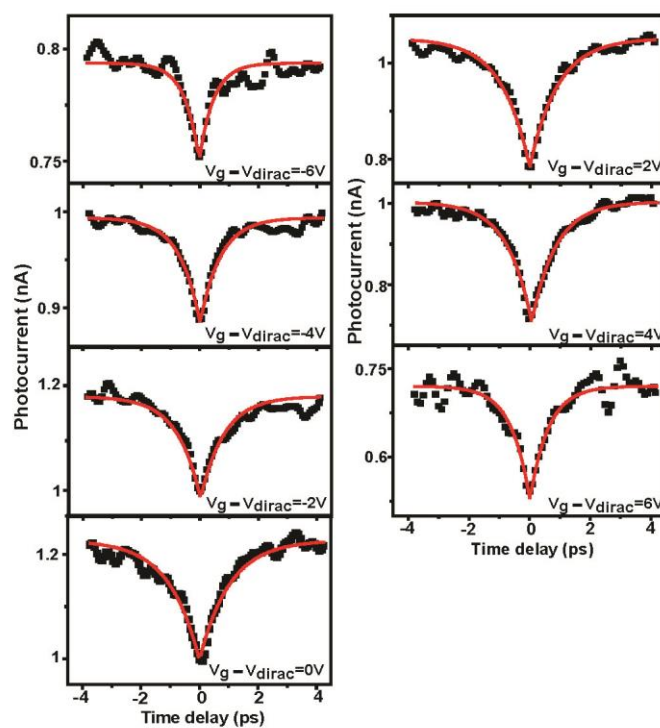
### Ultrafast pump probe measurements

Fig. S5 presents a schematic diagram of ultrafast pump probe setup. Laser pulses (150 fs pulse width) are generated from Ti-Sapphire laser with the repetition rate at 76 MHz and central wavelength at 800 nm. The generated femtosecond pulse train is then split into the probe (13.2 pJ) and pump (15.8 pJ) beam by a beam splitter (BS). The probe beam is reflected by a fixed mirror (M1) and modulated by the mechanical chopper (1.3 kHz). The pump beam is reflected by another mirror (M2), mounted on the motorized stage to induce a time delay between two pulses. Also, the polarization of pump beam is rotated by 90 degrees with respect to the probe beam in order to suppress the interference. Finally, two beams are collinear focused on the graphene device.

When measuring the ultrafast photoresponse from the device, two beams are focused on the metal/graphene interface and the change of short-circuit photocurrent as a function of the time delay is detected by using a lock-in amplifier referenced to the chopping frequency. As shown in Fig. S6, the magnitude of photocurrent decays by reducing the time delay between two pulses. Based on the drift-diffusion model, this decay curve is related to hot carrier cooling rate. However, we note there is no simply analytical relation between the magnitude of photocurrent and photocarrier temperature. Therefore, we fitted each decay curve with a single exponential decay, and the extracted lifetime from the exponential decay is defined as the response time in this work.



**Figure S5 Ultrafast pump probe spectroscopy.** This figure schematically shows the setup of ultrafast pump probe measurement.



**Figure S6 Ultrafast pump probe experimental results.** The figure shows the magnitude of photocurrent changes as a function of time delay. Also, different bottom gate voltages are applied in order to study the gate-dependent response time.

## Supplementary Section 6.

Table S1 List of Devices and Their Parameters

	Mobility ( $cm^2V^{-1}s^{-1}$ )		$E_f^0$ (eV)	Contact metal	Maximum Photocurrent (nA)	Polarity of Photocurrent
	$\mu_e$	$\mu_h$				
Device A	1095	1289	4.72	Titanium	3.3	Positive
Device B	820	611	4.28	Titanium	1.14	Negative
Device C	751	925	4.75	Palladium	5.13	Positive
Device D	705	976	4.25	Titanium	1.65	Positive
Device E	837	524	4.21	Titanium	2.61	Negative
Device F	1729	1021	4.59	Palladium	5.29	Negative
Device G	2331	2560	4.73	Titanium	3.27	Positive
Device H	2856	2387	4.47	Palladium	4.25	Negative
Device I	1721	2432	4.7	Titanium	7.56	Positive
Device J	705	865	4.69	Titanium	2.62	Positive
Device K	649	886	4.5	Palladium	3.43	Positive
Device L	975	1235	4.64	Palladium	5.25	Positive
Device M	1922	2169	4.74	Titanium	4.08	Positive
Device N	1191	1735	4.71	Titanium	4.22	Positive
Device O	900	1204	4.41	Palladium	5.62	Positive

$\mu_e$ , electron mobility;  $\mu_h$ , hole mobility;  $E_f^0$ , intrinsic Fermi level of graphene

In this table, the polarity and maximum photocurrent are extracted at the left contact from each graphene device.

The excitation pulse energy is  $\sim 19.7$  pJ for all the photocurrent measurements.

**References:**

- 1 Park, J.; Ahn, Y. H.; Ruiz-Vargas, C. *Nano Letters* **2009**, 9, 1742-1746.
- 2 Xia, F.; Mueller, T.; Golizadeh-Mojarad, R.; Freitag, M.; Lin, Y.-M.; Tsang, J.; Perebeinos, V.; Avouris, P. *Nano Letters* **2009**, 9, 1039-1044.
- 3 Liu, C.-H.; Dissanayake, N. M.; Lee, S.; Lee, K.; Zhong, Z. *Acs Nano* **2012**, 6, 7172-7176.
- 4 Xu, X. D.; Gabor, N. M.; Alden, J. S.; van der Zande, A. M.; McEuen, P. L. *Nano Lett.* **2010**, 10, 562-566.
- 5 Wang, Y.; Brar, V. W.; Shytov, A. V.; Wu, Q.; Regan, W.; Tsai, H. Z.; Zettl, A.; Levitov, L. S.; Crommie, M. F. *Nat. Phys.* **2012**, 8, 653-657.
- 6 Ruzicka, B. A.; Wang, S.; Werake, L. K.; Weintrub, B.; Loh, K. P.; Zhao, H. *Phys. Rev. B* **2010**, 82, 195414.
- 7 Lui, C. H.; Mak, K. F.; Shan, J.; Heinz, T. F. *Phys. Rev. Lett.* **2010**, 105, 127404.